

Commensurate-incommensurate transition in graphene on hexagonal boron nitride

C. R. Woods¹, L. Britnell¹, A. Eckmann², R. S. Ma³, J. C. Lu³, H. M. Guo³, X. Lin³, G. L. Yu¹, Y. Cao⁴, R. V. Gorbachev⁴, A. V. Kretinin¹, J. Park^{1,5}, L. A. Ponomarenko¹, M. I. Katsnelson⁶, Yu. N. Gornostyrev⁷, K. Watanabe⁸, T. Taniguchi⁸, C. Casiraghi², H.-J. Gao³, A. K. Geim⁴ and K. S. Novoselov^{1*}

When a crystal is subjected to a periodic potential, under certain circumstances it can adjust itself to follow the periodicity of the potential, resulting in a commensurate state. Of particular interest are topological defects between the two commensurate phases, such as solitons and domain walls. Here we report a commensurate-incommensurate transition for graphene on top of hexagonal boron nitride (hBN). Depending on the rotation angle between the lattices of the two crystals, graphene can either stretch to adapt to a slightly different hBN periodicity (for small angles, resulting in a commensurate state) or exhibit little adjustment (the incommensurate state). In the commensurate state, areas with matching lattice constants are separated by domain walls that accumulate the generated strain. Such soliton-like objects are not only of significant fundamental interest, but their presence could also explain recent experiments where electronic and optical properties of graphene-hBN heterostructures were observed to be considerably altered.

The classical system which is used to simulate commensurate-incommensurate transitions is a one-dimensional chain of elastically linked atoms in a background periodic potential—the Frenkel–Kontorova model¹. The two-dimensional (2D) version of the model^{2,3} can be applied to real-life systems, such as the surface reconstruction at the interface between two crystals (or between a crystal and a surface monolayer) with close atomic lattice periods^{4–7}. Commensurate-incommensurate transitions in 2D have been discussed^{5–8} and observed⁹ previously in systems such as adsorbed atoms on a surface of a crystal. Interestingly, the boundaries between the commensurate phases can be described in terms of topological defects. In the one-dimensional case such defects are usually described by solitons^{1,4,10}, whereas in 2D the language of misfit dislocations is commonly used¹¹. The ultimate way to observe such reconstruction would be by monitoring the behaviour of two 2D atomic crystals when placed in close contact.

Recent advances in the production of heterostructures based on 2D atomic crystals¹², and, in particular, the preparation¹³ and growth¹⁴ of graphene on hBN, allow us to revisit this problem. hBN has been originally used as a substrate^{13,15} and also an encapsulation layer¹⁶, which allows minimization of the detrimental influence of SiO₂ substrates, and, as a consequence, the achievement of spectacular electronic quality of the resulting graphene devices. Still, the van der Waals interaction between hBN and graphene, however weak, is not negligible (≈ 10 meV per carbon atom)¹⁷. The mismatch $\delta = a_{\text{hBN}}/a_{\text{G}} - 1 \approx 1.8\%$ between the lattice constants of hBN (a_{hBN}) and graphene (a_{G}) and the relative rotation angle φ between the graphene and hBN crystals lead to a hexagonal moiré pattern

(Fig. 1), which has been observed by scanning probe microscopy^{18,19}. The moiré potential acts on charge carriers in graphene, resulting in a modification of its electronic spectrum^{20–23}. So far it has been assumed that no structural changes occur in graphene after it is brought in contact with hBN.

In this paper we investigate (by atomic force microscopy (AFM), scanning tunnelling microscopy (STM) and Raman spectroscopy) the strain distribution in graphene on hBN for different misorientation angles between the two crystalline structures (which results in the variation of the period L of the moiré pattern). We observe a commensurate-incommensurate transition that occurs when φ is of the order of δ (that is, $\approx 1^\circ$). For $\varphi < \delta$ (large $L > 10$ nm), graphene stretches locally to achieve an energetically favourable state for van der Waals interactions with hBN, which results in relatively large areas of commensurate stacking and deformations concentrated in narrow strained regions (similar to soliton lattice formation in one dimension^{1,10}). For $\varphi > \delta$ (small moiré periodicity), graphene and hBN lattices remain unsynchronized and there are no distinct regions with accumulated strain.

Our samples are fabricated by the dry transfer method, described in detail in refs 16,24. In brief, graphene is prepared by micromechanical cleavage²⁵ on top of a polymer film consisting of two sacrificial layers. By dissolving one of them, graphene supported by the second layer can be transferred on top of a relatively thick (> 10 nm) crystal of hBN. Then the second sacrificial layer is also removed and the assembly is annealed in a forming gas at a temperature of $\sim 250^\circ\text{C}$ to achieve an atomically clean interface²⁶.

¹School of Physics and Astronomy, University of Manchester, Manchester M13 9PL, UK, ²School of Chemistry and Photon Science Institute, University of Manchester, Oxford Road, Manchester, M13 9PL, UK, ³Institute of Physics and University of Chinese Academy of Sciences, Chinese Academy of Sciences, Beijing 100190, China, ⁴Centre for Mesoscience and Nanotechnology, University of Manchester, Manchester M13 9PL, UK, ⁵Center for Nano-metrology, Korea Research Institute of Standards and Science, 267 Gajeong Ro, Yuseong-Gu, Daejeon, 305-340, Republic of Korea, ⁶Institute for Molecules and Materials, Radboud University of Nijmegen, Nijmegen 6525 AJ, The Netherlands, ⁷Institute of Quantum Materials Science, Ekaterinburg 620075, Russia, ⁸National Institute for Materials Science, 1-1 Namiki, Tsukuba 305-0044, Japan. *e-mail: kostya@manchester.ac.uk

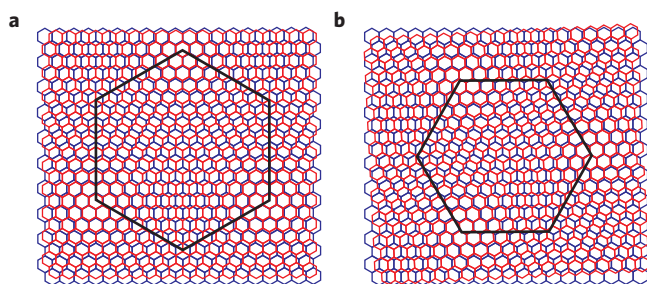


Figure 1 | Schematic representation of the moiré pattern of graphene (red) on hBN (blue). **a** Relative rotation angle between the crystals $\varphi = 0^\circ$. **b** Relative rotation angle between the crystals $\varphi = 3^\circ \approx 0.052$ rad. The mismatch between the lattices is exaggerated ($\sim 10\%$). Black hexagons mark the moiré plaquette.

We control φ with $\sim 0.5^\circ$ precision, as described previously²⁰. In some of the experiments described below, we have used structures with another hBN crystal (1–5 nm thick) added on top to encapsulate graphene. The quality of the graphene–hBN interface and the presence of the moiré pattern have been confirmed by transport measurements and by conductive AFM measurements²⁰.

We studied our samples by AFM (in various modes) and Raman spectroscopy. No moiré pattern has been observed in the AFM topography signal—neither in contact nor in tapping modes (precision ~ 50 pm). At the same time, the moiré pattern can be seen in the friction signal, which may indicate areas with different adhesion²⁷. To elaborate on this finding we have measured force curves at different positions on the surface. To do that we have used PeakForce Tapping AFM (ref. 28), which allows us to extract local elastic constants, including the Young's modulus and adhesion^{29,30}.

First we investigate a structure with $\varphi \sim 1.5^\circ$ and $L \sim 8$ nm (Fig. 2a,c,e). The moiré pattern is clearly seen in the conductive AFM (Fig. 2a) and Young's modulus signals (Fig. 2c). There is no signal in the adhesion channel.

The pattern of Young's modulus distribution for the $L = 8$ nm sample has a hexagonal symmetry with smooth changes across each moiré unit cell. Figure 2e shows that the cross-section is close to the sinusoidal shape. Overall, it follows the prediction of ref. 17, where both the Young's modulus and the adhesion follow a characteristic hexagonal structure. The reason we see no pattern in the adhesion signal is probably because the adhesion between graphene and hBN is much larger than the adhesion between the AFM tip and graphene.

The situation is very different for the sample with $\varphi \sim 0^\circ$ and $L = 14$ nm. The pattern of the Young's modulus signal is still hexagonal, but it changes abruptly in space (Fig. 2d), with large areas of low, practically constant Young's modulus separated by narrow regions of high modulus (domain walls, seen as bright lines on Fig. 2d). The cross-section reveals that the latter is only ~ 2 nm wide. Similar behaviour is observed by conductive AFM: smooth variations for 8 nm moiré samples and sharp features separating domains of practically constant conductivity in the 14 nm moiré patterns. Note that the hexagonal symmetry is broken, with every second vertex being much brighter. It might indicate a specific stacking between graphene and hBN, or a concentration of strain, which alters the electronic structure through the effect of a pseudo-magnetic field^{31,32}.

We summarize this finding in Fig. 2g, where we plot the ratio between the FWHM of the peak in the Young's modulus to the period of the moiré pattern for the same sample. For samples with $L < 10$ nm this ratio saturates at 0.5—as it should if there is no reconstruction of the graphene lattice (Fig. 2e). For our best aligned samples ($L \sim 14$ nm), this ratio is close to 0.1. The relative width of the peak in the Young's modulus grows gradually as

the alignment becomes less perfect and, at $L \sim 10$ nm, the pattern suddenly becomes practically sinusoidal (the ratio is ~ 0.5).

Such a change in behaviour can be explained by the commensurate–incommensurate transition as a function of φ . The basic physics behind such transitions is as follows^{4,8,10}: if the relative rotation angle between the two crystals is small (large period of the moiré pattern), it becomes energetically favourable to adjust the two lattices to become commensurate, losing in elastic energy but gaining in van der Waals energy. The latter decreases if preferred atomic positions are achieved over the whole area. When φ increases past some critical value (so that the period of the moiré pattern becomes small), the gain in the van der Waals energy can no longer compensate for the elastic energy and the two crystals act independently, forming an incommensurate state.

In principle it is possible to imagine a situation when the commensurate state would extend across the whole interface between the two crystals and the crystals would be uniformly stretched or compressed (it would happen, for instance, if the gain in van der Waals energy is sufficiently large and in the absence of the 3D elastic fields in the substrate). In our case, however, when graphene is mechanically deposited on hBN, such uniform stretching of graphene would require its macroscopic motion. In practice, graphene is always pinned by imperfections, so its size is fixed. This leads to the formation of domains (where graphene and hBN are commensurate) and domain walls (where graphene is compressed and the stacking order changes rapidly in space). Note that in such a scenario the overall period of the moiré pattern does not change, but the strains change sign in space.

In the Frenkel–Kontorova model the adjacent regions of commensurate phase (when the atoms fall into the minima of the background periodic potential—the so-called Peierls potential¹) are separated by solitons. The width of the soliton is given by $\lambda \propto (Y/\gamma)^{1/2}$, where Y is the Young's modulus and γ is the depth of the background periodic potential. The commensurate–incommensurate transition (although it is not necessarily a phase transition in the one-dimensional model) occurs when the size of the soliton becomes comparable to the size of the commensurate region, such as for very stiff crystals (large Y) or for a very shallow background potential (small γ).

The 2D case of graphene on hBN can be qualitatively traced back to the Frenkel–Kontorova model, with the role of solitons (topological defects) being played by a system of screw and edge dislocations (the former are associated with rotations whereas the latter are introduced by a lattice misfit¹¹; see also Supplementary Information) between graphene and the hBN lattice. Note that, even though the language of dislocations is used here, graphene is still defect-free and the dislocations reflect only the mismatch in the lattice constants of graphene and hBN in a certain direction. As the rotation angle increases, two processes occur: the distance between the dislocations becomes smaller (shortening of the period of the moiré pattern) and the width of the dislocation cores increases owing to a flattening of the effective Peierls potential. The latter is illustrated in Fig. 1: for $\varphi = 0$ the moiré plaquette is aligned with the crystallographic directions of graphene and hBN, and thus the Peierls potential is atomically sharp. At the same time, for any finite φ the moiré plaquette is misaligned with respect to the crystallographic directions, and thus the Peierls potential has a complicated shape, with a period much larger than the lattice period. As a result, when the rotation angle reaches a value of the order of the lattice misfit (0.018) the dislocation cores become as large as the moiré period itself. This is nothing but the commensurate–incommensurate transition: for smaller rotation angles, all lattice misfit is concentrated in relatively narrow, well-defined dislocation walls, whereas for larger misorientation, the angular and lattice misfit is more or less uniformly distributed through the whole system. Detailed

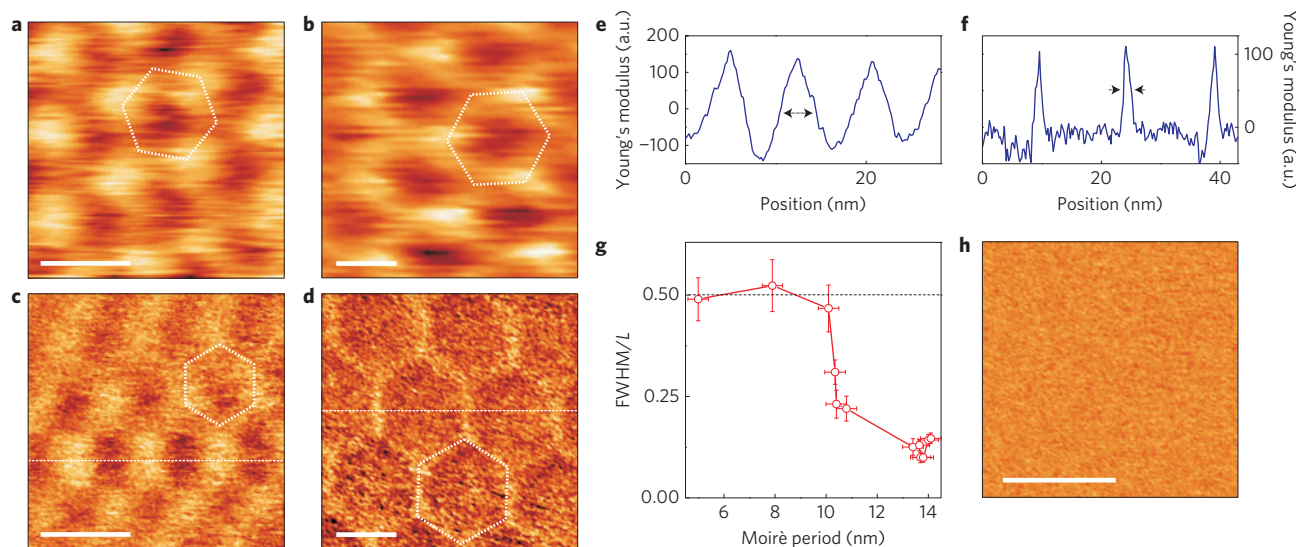


Figure 2 | Experimental observation of moiré patterns for graphene-on-hBN samples with different relative orientation angles. **a** Local resistance measured by conductive AFM for one of our graphene-on-hBN samples with an 8 nm moiré pattern. Colour scale: from white to black is from 105 to 120 k Ω . **b** Same as in **a** for a sample with a 14 nm moiré periodicity — the crystallographic axes of graphene and hBN are practically aligned. Colour scale: from 135 to 170 k Ω . **c,d**, Young's modulus distribution, measured in the PeakForce mode, for structures with 8 and 14 nm moiré patterns, respectively. **e,f**, Cross-sections of the Young's modulus distribution taken along the dashed lines in **c** and **d**, respectively, and averaged over ten scanning lines (approx. 2.5 nm). **g**, Ratio between FWHM of the peak in the Young's modulus distribution (as marked by arrows in **e** and **f**) and the period of the moiré structure L , as a function of the period of the moiré structure for several of our samples. The error bars are determined by the distribution of the sizes of the domains and domain walls measured over an area of $0.5\mu\text{m} \times 0.5\mu\text{m}$. **h**, Young's modulus distribution across an unaligned sample (angle between graphene and hBN $\sim 15^\circ$). Scale bars for **a,b,c,d** and **h** are 10 nm.

quantitative analysis demonstrates that the switchover between commensurate and incommensurate phases indeed happens through a phase transition (see Supplementary Information).

To test this theory we directly measured the interatomic distances at different parts of the moiré pattern with STM (Fig. 3). The STM image shows a reconstructed moiré pattern (narrow domain wall-like objects) on all three tested samples, which is in agreement with previous STM data^{18,19}. We analysed the interatomic distances at different areas of the moiré pattern (Fig. 3b), namely: at the body of the hexagon (dark areas in Fig. 3a,b, marked by the black square in Fig. 3b), at the vertexes of the hexagons (where the three domain walls merge, marked by red and green squares in Fig. 3b) and in the middle of the domain walls (blue square in Fig. 3b). The interatomic distance was analysed by taking a 2D Fourier transform and observing the positions of the first-order peaks. We took care to compare the positions of peaks that correspond to the same crystallographic directions (Fig. 3c). In this way we avoided the artefacts associated with any thermal drift.

Throughout all our samples we found that the interatomic distances within the body of the domains are consistently larger than those within the domain walls (Fig. 3d). The difference is $2.0 \pm 0.6\%$ (see Supplementary Information for further details). The sign and the value of the effect are consistent with the above theory. The fact that the lattice extension for the domain area (marked by the black square in Fig. 3b) with respect to the other parts of the moiré pattern is larger than δ suggests that the lattice within the domain walls (areas marked by the blue, red and green boxes in Fig. 3b) is most probably compressed. Unfortunately, at this stage we cannot say anything about the specific direction of the strain within the domain walls, as we are working at the resolution limit of our STM.

It is clear that the strain distribution in graphene on hBN is quite different for commensurate and incommensurate states. Recently, it has been demonstrated that the FWHM of the Raman 2D peak for graphene with $L = 14$ nm is about 50% larger than that for samples with the 8 nm moiré pattern³³ (the result is reproduced in Fig. 4a).

Such behaviour could be explained by elastic deformations in the aligned graphene³⁴.

One can expect that the commensurate state of graphene on hBN can be suppressed by placing an additional hBN crystal on top. If the top hBN is rotated by a large angle ($\varphi > 5^\circ$), graphene would experience an additional van der Waals potential with a short L (ref. 18). This should reduce the influence of the bottom van der Waals potential and the combined effect may lead to the disappearance of the commensurate state.

We have checked this behaviour by producing encapsulated graphene samples where graphene is aligned relative to the bottom hBN, and the top hBN rotated by approximately 15° with respect to the crystallographic directions of graphene (the top hBN covers the graphene only partially). It is impossible to observe the moiré pattern by AFM on the covered graphene, so only a comparative study of the Raman signal on the covered and uncovered graphene has been performed. The uncovered graphene has been found to be in the commensurate state, as confirmed by both AFM and Raman. As for the covered graphene, the Raman peak is found not to be broadened in comparison with graphene on hBN with the 8 nm moiré pattern. This means that encapsulated graphene remains in an incommensurate state even if thoroughly aligned.

The observed strain in graphene aligned on hBN and the quenching of the commensurate state in encapsulated aligned samples can explain recent observations of a gap opening in some graphene-on-hBN devices²² and its absence in others^{13,15,16}. The difference between the two sets of devices was the placement of hBN crystals on top of the latter devices. To confirm this hypothesis, we have prepared similar sets of aligned graphene devices and studied their transport properties. The devices were standard Hall bars, and L was approximately the same (14 nm) as found from the gate voltage at which the secondary Dirac points occur²⁰.

In the non-encapsulated devices the commensurate transition has been observed by AFM and Raman spectroscopy. These

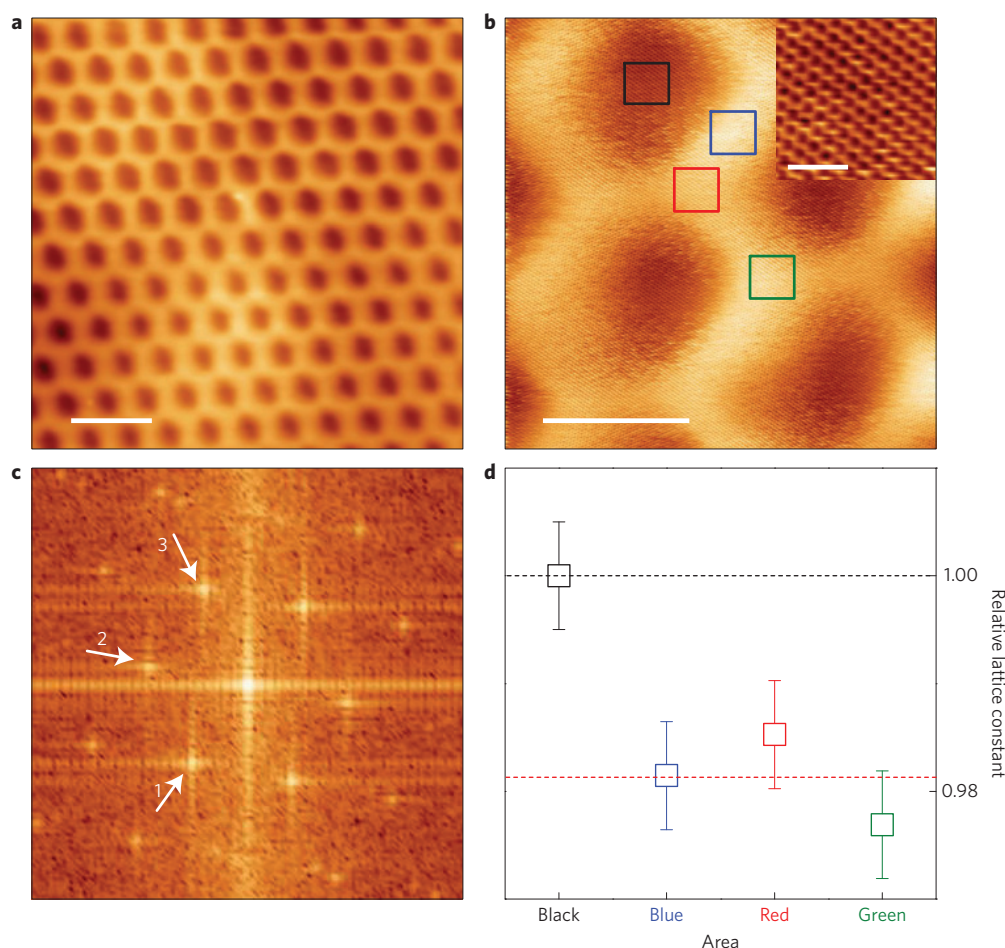


Figure 3 | STM measurements on one of our fully aligned graphene-on-hBN samples. **a**, STM image of one of our aligned samples. A moiré pattern is clearly visible. Scale bar, 30 nm. The sample bias is -0.1 V and the tunnelling current is 300 pA. **b**, Same as in **a**, but at a higher magnification. Both the moiré pattern and the atomic structure are resolved. Scale bar, 10 nm. The sample bias is -0.1 V and the tunnelling current is 800 pA. Coloured squares (3 nm in size) indicate the fragments used for Fourier transformation to determine the interatomic distance. Inset: a blow up of the area marked by the black square, with the atomic structure clearly visible. Scale bar, 1 nm. **c**, Example of the Fourier transform of the atomically resolved structure. In this case, as the starting image we used the $3\text{ nm} \times 3\text{ nm}$ square image at the vertex of the hexagonal pattern (red square in **b**). The width of the panel is 19 nm^{-1} . **d**, Relative lattice constants (with respect to those measured for the area marked by the black square in **b**) for different areas within the moiré pattern (colours corresponds to those in **b**), obtained from the positions of the first-order peaks in **c** and averaged over the three directions. The error bars are determined by the width of the peaks in the FFT of the atomically resolved structures in **c** and by the spread across the three directions as marked in **c**.

devices exhibit an insulating behaviour at the main neutrality point (Fig. 5a). The associated gap, Δ , is estimated as ≈ 360 K by fitting the high-temperature data with the Arrhenius law (Fig. 5c). At temperatures below 60 K the insulating behaviour shows a slower dependence, which may indicate the onset of hopping conductivity. The size of the gap is similar to that reported previously for aligned but not encapsulated graphene²². In contrast, our encapsulated samples, which are identified by Raman spectroscopy as being in the incommensurate state, exhibit a weak temperature dependence, with a resistivity of the order of several k Ω at low temperatures (Fig. 5b). This leaves a possibility of only a small gap at the main neutrality point, much smaller than that observed in non-encapsulated devices. Furthermore, we have studied tens of graphene-on-hBN devices (encapsulated and open) and never observed a gap in those with $L < 10\text{ nm}$ ($\varphi \sim 1^\circ$).

Therefore, the gap at the main Dirac point can be associated with the commensurate state. The sublattice symmetry in graphene is locally broken owing to the proximity to hBN. However, the resulting local gaps vary spatially, and the global transport gap may be small as a result of averaging^{17,35}. In the commensurate state, large areas of graphene would have the same crystal structure as

hBN and, therefore, a constant magnitude of the gap. This would strongly enhance the global transport gap and could be responsible for the observed large Δ . An alternative explanation would be that the transport is limited by percolation through the system of the ‘domain walls’. The insulating behaviour in such regions (Fig. 2d) could be due to a strong inhomogeneous strain that leads to energy gaps which are often interpreted in terms of large pseudo-magnetic fields^{31,32,36}.

Finally, we would like to discuss the possible microscopic strain distributions for our samples in the commensurate state. Two structures for the boundary between adjacent commensurate domains are possible: those which accommodate tensile strain and those which accommodate shear strain. The shear strain is, however, more energetically favourable, as the shear modulus is half the Young’s modulus³⁷. This observation is also supported by our Raman measurements: a tensile-type of strain distribution would require a very large strain accumulated within the narrow boundary (of the order of 10%), which would be observed as much larger broadening of the Raman 2D peak. Similar conclusions can be drawn from the STM results: a tensile-type of strain distribution would result in a much larger difference in the lattice constants

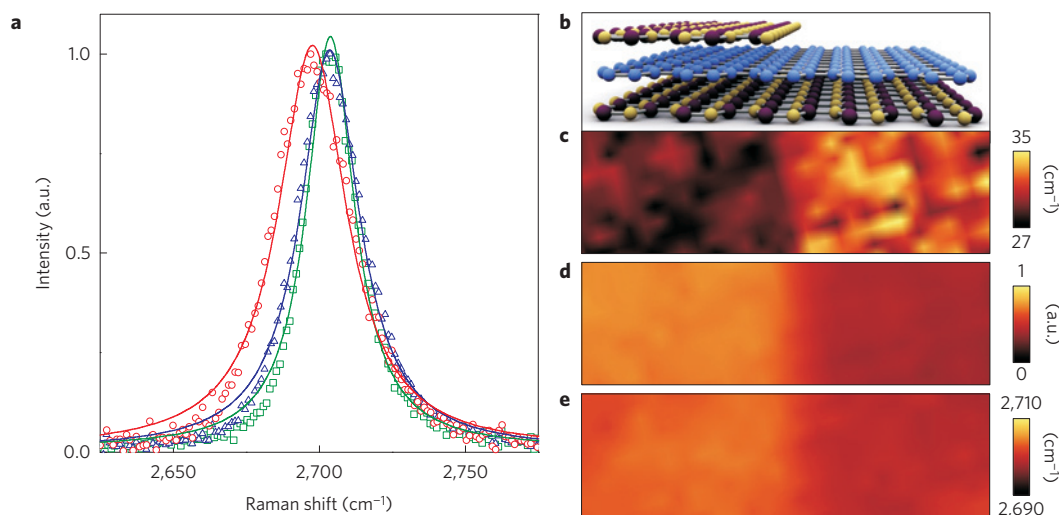


Figure 4 | Raman measurements on aligned and misaligned graphene on hBN samples. **a**, Raman 2D peak for various graphene samples on hBN samples. The data are normalized by the amplitude of the 2D peak. Symbols are the experimental data points, with lines of the corresponding Lorentzian fit in the respective colour. Red circles and line: graphene on hBN with $L \approx 14$ nm, non-encapsulated. Blue triangles and line: the same L but encapsulated. Green squares and line: $L \approx 8$ nm, non-encapsulated. **b**, Schematic representation of one of our devices with graphene partially encapsulated. **c**, Spatial map of the FWHM of the 2D peak for a graphene-on-hBN sample with the period of moiré pattern 14 nm. The left half of the sample is encapsulated with a few layers of hBN. Crystallographic directions of the top hBN are rotated by approximately 15° with respect to those of graphene. **d**, Spatial map of the amplitude of the 2D peak for the same sample as in **c**, normalized to the amplitude of the G peak. **e**, Spatial map of the position of the 2D peak for the same sample as in **c**. Laser excitation is 488 nm for all Raman data. The width of panels **c**, **d** and **e** is 3 μ m.

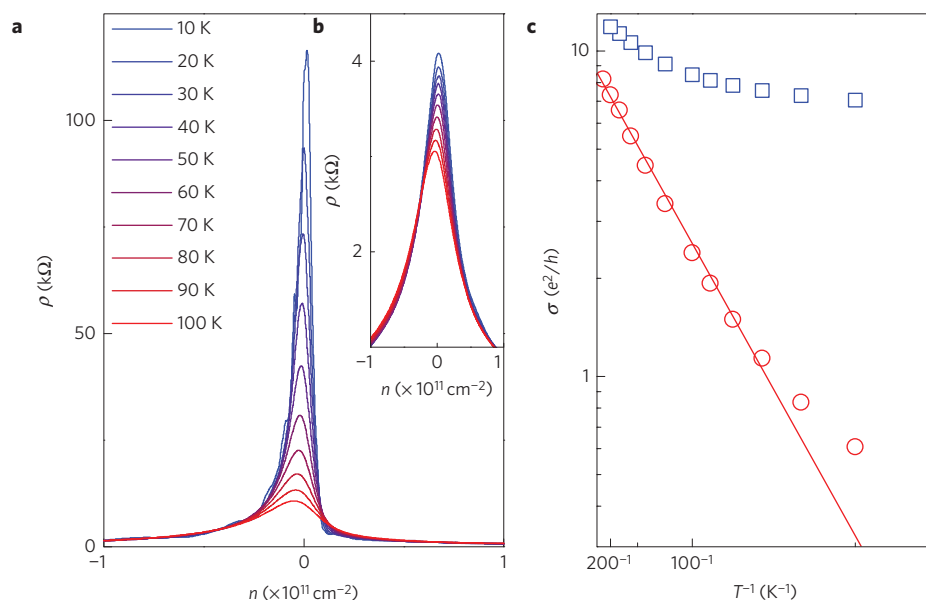


Figure 5 | Transport measurements and estimation of a gap on encapsulated and non-encapsulated samples. **a**, Longitudinal resistivity (ρ) as a function of carrier concentration (n) for non-encapsulated graphene on hBN with the 14 nm moiré pattern for a range of temperatures. **b** Same as **a** for an encapsulated device with the 14 nm moiré pattern. **c** Temperature dependence of the conductivity minimum (σ) for the samples in **a** (red circles) and in **b** (blue squares). The red line is a guide for an eye, yielding $\Delta/2 \approx 180$ K.

between the domains and the domain walls. The possibility of generating a periodic distribution of shear strain allows for local strain concentration and calls for further study.

Received 5 February 2014; accepted 19 March 2014;
published online 28 April 2014

References

1. Braun, O. M. & Kivshar, Y. S. *The Frenkel–Kontorova Model: Concepts, Methods, and Applications* 1st edn (Springer-Verlag, 2004).
2. Pokrovsky, V. L. & Talapov, A. L. Phase-transitions and oscillation spectra of almost commensurate structures. *Zh. Eksp. Teor. Fiz.* **75**, 1151–1157 (1978).
3. Gornostyrev, Y. N., Katsnelson, M. I., Kravtsov, A. V. & Trefilov, A. V. Fluctuation-induced nucleation and dynamics of kinks on dislocation: Soliton and oscillation regimes in the two-dimensional Frenkel–Kontorova model. *Phys. Rev. B* **60**, 1013–1018 (1999).
4. Frank, F. C. & van der Merwe, J. H. One-dimensional dislocations. I. Static theory. *Proc. R. Soc. Lond. A* **198**, 205–216 (1949).
5. Rockett, A. & Kiely, C. J. Energetics of misfit-dislocation and threading-dislocation arrays in heteroepitaxial films. *Phys. Rev. B* **44**, 1154–1162 (1991).

6. Pushpa, R. & Narasimhan, S. Stars and stripes. Nanoscale misfit dislocation patterns on surfaces. *Pure Appl. Chem.* **74**, 1663–1671 (2002).
7. Chen, S. D., Zhou, Y. K. & Soh, A. K. Molecular dynamics simulations of mechanical properties for Cu(001)/Ni(001) twist boundaries. *Comput. Mater. Sci.* **61**, 239–242 (2012).
8. Pokrovsky, V. L. & Talapov, A. L. Ground-state, spectrum, and phase-diagram of 2-dimensional incommensurate crystals. *Phys. Rev. Lett.* **42**, 65–67 (1979).
9. Fain, S. C., Chinn, M. D. & Diehl, R. D. Commensurate–incommensurate transition of solid krypton monolayers on graphite. *Phys. Rev. B* **21**, 4170–4172 (1980).
10. Bak, P. Commensurate phases, incommensurate phases and the Devil's staircase. *Rep. Prog. Phys.* **45**, 587–629 (1982).
11. Hirth, J. P. & Lothe, J. *Theory of Dislocations* 2nd edn 872, (Krieger Publishing Company, 1982).
12. Geim, A. K. & Grigorieva, I. V. Van der Waals heterostructures. *Nature* **499**, 419–425 (2013).
13. Dean, C. R. *et al.* Boron nitride substrates for high-quality graphene electronics. *Nature Nanotech.* **5**, 172–176 (2010).
14. Tang, S. J. *et al.* Precisely aligned graphene grown on hexagonal boron nitride by catalyst free chemical vapor deposition. *Sci. Rep.* **3**, 2666 (2013).
15. Dean, C. R. *et al.* Multicomponent fractional quantum Hall effect in graphene. *Nature Phys.* **7**, 693–696 (2011).
16. Mayorov, A. S. *et al.* Micrometer-scale ballistic transport in encapsulated graphene at room temperature. *Nano Lett.* **11**, 2396–2399 (2011).
17. Sachs, B., Wehling, T. O., Katsnelson, M. I. & Lichtenstein, A. I. Adhesion and electronic structure of graphene on hexagonal boron nitride substrates. *Phys. Rev. B* **84**, 195414 (2011).
18. Xue, J. M. *et al.* Scanning tunnelling microscopy and spectroscopy of ultra-flat graphene on hexagonal boron nitride. *Nature Mater.* **10**, 282–285 (2011).
19. Yankowitz, M. *et al.* Emergence of superlattice Dirac points in graphene on hexagonal boron nitride. *Nature Phys.* **8**, 382–386 (2012).
20. Ponomarenko, L. A. *et al.* Cloning of Dirac fermions in graphene superlattices. *Nature* **497**, 594–597 (2013).
21. Dean, C. R. *et al.* Hofstadter's butterfly and the fractal quantum Hall effect in moiré superlattices. *Nature* **497**, 598–602 (2013).
22. Hunt, B. *et al.* Massive Dirac fermions and Hofstadter butterfly in a van der Waals heterostructure. *Science* **340**, 1427–1430 (2013).
23. Wallbank, J. R., Patel, A. A., Mucha-Kruczynski, M., Geim, A. K. & Falko, V. I. Generic miniband structure of graphene on a hexagonal substrate. *Phys. Rev. B* **87**, 245408 (2013).
24. Ponomarenko, L. A. *et al.* Tunable metal–insulator transition in double-layer graphene heterostructures. *Nature Phys.* **7**, 958–961 (2011).
25. Novoselov, K. S. *et al.* Electric field effect in atomically thin carbon films. *Science* **306**, 666–669 (2004).
26. Haigh, S. J. *et al.* Cross-sectional imaging of individual layers and buried interfaces of graphene-based heterostructures and superlattices. *Nature Mater.* **11**, 764–767 (2012).
27. Lee, C. *et al.* Frictional characteristics of atomically thin sheets. *Science* **328**, 76–80 (2010).
28. Pittenger, B. B., Erina, N. & Su, C. Quantitative mechanical property mapping at the nanoscale with PeakForce QNM (Bruker, 2012); http://www.bruker.com/fileadmin/user_upload/8-PDF-Docs/SurfaceAnalysis/AFM/ApplicationNotes/AN128-RevB0-Quantitative_Mechanical_Property_Mapping_at_the_Nanoscale_with_PeakForceQNM-AppNote.pdf
29. Derjaguin, B. V., Muller, V. M. & Toporov, Y. P. Effect of contact deformation on adhesion of particles. *J. Colloid Interf. Sci.* **53**, 314–326 (1975).
30. Tamayo, J. & Garcia, R. Effects of elastic and inelastic interactions on phase contrast images in tapping-mode scanning force microscopy. *Appl. Phys. Lett.* **71**, 2394–2396 (1997).
31. Guinea, F., Katsnelson, M. I. & Geim, A. K. Energy gaps and a zero-field quantum Hall effect in graphene by strain engineering. *Nature Phys.* **6**, 30–33 (2010).
32. Guinea, F., Geim, A. K., Katsnelson, M. I. & Novoselov, K. S. Generating quantizing pseudomagnetic fields by bending graphene ribbons. *Phys. Rev. B* **81**, 035408 (2010).
33. Eckmann, A. *et al.* Raman fingerprint of aligned graphene/h-BN superlattices. *Nano Lett.* **13**, 5242–5246 (2013).
34. Mohiuddin, T. M. G. *et al.* Uniaxial strain in graphene by Raman spectroscopy: G peak splitting, Grüneisen parameters, and sample orientation. *Phys. Rev. B* **79**, 205433 (2009).
35. Song, J. C. W., Shytov, A. V. & Levitov, L. S. Engineering interaction effects and gap opening in graphene superlattices. *Phys. Rev. Lett.* **111**, 266801 (2012).
36. Low, T., Guinea, F. & Katsnelson, M. I. Gaps tunable by electrostatic gates in strained graphene. *Phys. Rev. B* **83**, 195436 (2011).
37. Zakharchenko, K. V., Katsnelson, M. I. & Fasolino, A. Finite temperature lattice properties of graphene beyond the quasiharmonic approximation. *Phys. Rev. Lett.* **102**, 046808 (2009).

Acknowledgements

This work was supported by the European Research Council, Graphene Flagship, Engineering and Physical Sciences Research Council (UK), the Royal Society, US Office of Naval Research, US Air Force Office of Scientific Research, US Army Research Office, the MOST of China (No. 2013CBA01600) and the Körber Foundation. We are grateful to L. Levitov for useful discussions.

Author contributions

C.R.W. prepared the samples and did the majority of AFM and Raman experiments. L.B. and A.E. contributed to AFM and Raman experiments. R.S.M., J.C.L., H.M.G. and X.L. did the STM experiments. G.L.Y. and L.A.P. did the transport experiments. Y.C., R.V.G., A.V.K. and J.P. produced experimental samples. M.I.K. and Y.N.G. produced the theoretical analysis. K.W. and T.T. provided hBN. C.C. coordinated and analysed the Raman experiments. H.-J.G. coordinated and analyzed the STM experiments. A.K.G. and K.S.N. initiated and coordinated the work, participated in the experiments, analysed data, and wrote the manuscript.

Additional information

Supplementary information is available in the [online version of the paper](#). Reprints and permissions information is available online at www.nature.com/reprints. Correspondence and requests for materials should be addressed to K.S.N.

Competing financial interests

The authors declare no competing financial interests.

Commensurate-incommensurate transition in graphene on hexagonal boron nitride

Supporting online information

C. R. Woods¹, L. Britnell¹, A. Eckmann², R. S. Ma³, J. C. Lu³, H. M. Guo³, X. Lin³, G. L. Yu¹, Y. Cao,⁴ R. V. Gorbachev⁴, A.V. Kretinin¹, J. Park^{1,5}, L. A. Ponomarenko¹, M. I. Katsnelson⁶, Yu. N. Gornostyrev⁷, K. Watanabe⁸, T. Taniguchi⁸, C. Casiraghi², H. -J. Gao³, A. K. Geim⁴, K. S. Novoselov¹

¹*School of Physics and Astronomy, University of Manchester, Manchester M13 9PL, UK.*

²*School of Chemistry and Photon Science Institute, University of Manchester, Oxford Road, Manchester, M13 9PL, UK.*

³*Beijing National Laboratory of Condensed Matter Physics, Institute of Physics, Chinese Academy of Sciences, Beijing 100190, China*

⁴*Centre for Mesoscience and Nanotechnology, University of Manchester, Manchester M13 9PL, UK.*

⁵*Center for Nano-metrology, Korea Research Institute of Standards and Science, 267 Gajeong Ro, Yuseong-Gu, Daejeon, 305-340, Republic of Korea.*

⁶*Institute for Molecules and Materials, Radboud University of Nijmegen, Nijmegen 6525 AJ, The Netherlands.*

⁷*Institute of Quantum Materials Science, Ekaterinburg 620075, Russia*

⁸*National Institute for Materials Science, 1-1 Namiki, Tsukuba 305-0044, Japan*

Commensurate-incommensurate transition

Conditions of conjugation of two half spaces in a crystal have been discussed long ago in the context of grain boundaries [1,2]. The situation when a half of space is rotated (at angle ϕ) with respect to another half of space is called a twist grain boundary. There are two canonical ways to describe this situation. The first one is the simplest picture of a coincidence site lattice (CSL) [2] where one just rotates and puts one lattice onto the other without atomic relaxation; it corresponds to the moiré description used in previous works on graphene on hexagonal boron nitride (hBN) [3-6]. The second approach is based on the theory of dislocations [1]. Namely, one introduces two systems of screw dislocations with their axes (and, therefore, Burgers vectors \vec{b} which, for screw dislocations, are parallel to the axes) normal to the rotation axis. After this, the interface should be reconstructed to minimize the total energy. This reconstruction is well known for the one-dimensional case of two interacting chains with the lattice misfit where it results in a formation of soliton lattice [7,8]. This language is frequently used for a monolayer of adsorbed atoms rotated with respect to the host crystal [9-12].

The moiré pattern typical for the graphene-hBN system [3-6] arises naturally for a completely different situation, namely, in computer simulations for metals, see, e.g., Fig.5 of Ref. [10]. The description of the moiré pattern by the wave vector $\vec{k} = \vec{g} - \vec{g}'$ where \vec{g}, \vec{g}' are the shortest reciprocal lattice vectors of graphene and hBN, respectively [3] agrees naturally with the dislocation picture. The main difference between these two languages is that CLS assumes a matching of the layers only for special sites with the period $2\pi/k$, whereas in the dislocation pictures it takes place almost everywhere, except the dislocation cores. Thus, the description of rotated layers in terms of dislocations corresponds to *relaxed* moiré [9].

Keeping in mind applications to graphene-hBN, we consider only the case when the energy of interlayer (van der Waals) interaction V is much weaker than the cohesive energy within the layer and the misfit of lattice constant $b-a$ is small in comparison with a and b . Then, the interface structure results from an interplay of the van der Waals and elastic energies which are characterized by the parameters V and $E_{el} \approx Y(b-a)^2/2$, respectively (Y is the in-layer Young modulus). When $E_{el} \gg V$ the CSL picture (a naïve, that is, unreconstructed, moiré picture) with two incommensurate periods is energetically favorable but in the opposite case $E_{el} \ll V$ the lattice constants want to be equal to optimize the van der Waals energy, all lattice misfit being focused into “soliton lattice” with large commensurate regions between narrow solitons [8]. The “commensurate-incommensurate transition” takes place at $E_{el} \approx V$. The dislocation picture described above is a two-dimensional analog of the soliton lattice regime, and the commensurate-incommensurate transition at the change of misfit has been observed in many simulations for an adsorbed monolayer at metal and semiconductor surfaces [9-12]. For graphene-hBN system a typical energy of van der Waals interactions estimated as a difference between the total energies for A-B and A-A stacking corresponds to 20 meV and is slightly larger than the corresponding energy of elastic distortions involved in the formation of a moiré pattern [13]. In terms of dislocations, the “commensurate” (“soliton lattice”) phase corresponds to the situation of narrow dislocation cores, the core size is much smaller than the interdislocation distance. The commensurate-incommensurate transition corresponds to the case of overlapped cores when the description in terms of dislocations becomes meaningless. This can happen for both the decrease of the interdislocation distance and the increase for the core width; as we will see below both factors are relevant.

For triangular Bravais lattices the twist of top layers can be described by a superposition of two arrays of screw dislocations with the Burgers vectors $\vec{b}_1 = a(1,0)$, $\vec{b}_2 = a/2(1, -\sqrt{3})$ as shown in Supplementary fig. 1a, where a is the lattice constant. The distance between dislocations in each array is $\lambda = b / \left(2 \sin \frac{\phi}{2} \right)$, where ϕ is the rotation angle. Note that for the case of tilt grain boundaries one has to introduce a family of edge dislocations, with the same expression for the interdislocation distance (in that case ϕ is the tilting angle) [1,2]. Reaction between crossed dislocations $\vec{b}_1 + \vec{b}_2 \rightarrow \vec{b}_3$ is energetically favorable [1] and results in a formation of the hexagonal network (Supplementary fig. 1b); each segment of the network represents the screw dislocation, and the conservation equation for Burgers vector takes place in each triple joint. This dislocation networks (we will call them twist dislocations) determine a (plastic) rotation of the upper layer with respect to the lower one, the inner region of each hexagon being rotated in the opposite direction providing a complete matching

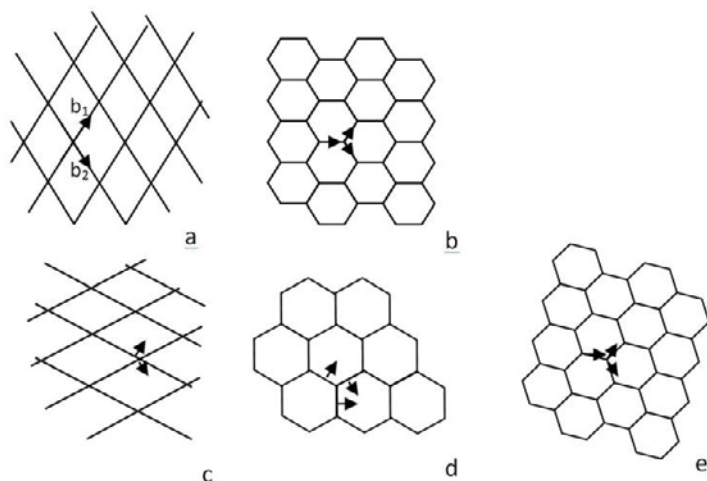


Fig. S1 - Dislocations arrays providing a rotation (a,b) and compensation of lattice misfit (c,d) for the graphene layer on hexagonal boron nitride. Lines correspond to dislocation axes and arrows to the Burgers vectors. Reactions between screw (a) or edge (c) dislocations $\vec{b}_1 + \vec{b}_2 \rightarrow \vec{b}_3$ lead to a formation of hexagonal networks (b) and (d). The hexagonal network at the figure (e) is obtained by a rotation of the network (b) by the angle α (S2) with the same directions of the Burgers vectors and provides both the twist of graphene layer and compensation of the lattice misfit everywhere except the dislocation walls forming the network.

screw (Fig. S1b) and edge (Fig. S1c) dislocations. Numerical simulation [10,12] shows that this superposition results in a hexagonal network of dislocations obtained by a rotation of the network of twist dislocations by the angle of rotation of the dislocation network α (which is defined explicitly below), keeping unchanged the directions of the Burgers vector with respect to the graphene lattice. The resulting network (Fig. S1e) consists of the dislocations with both screw and edge components providing both rotation and compensation of the lattice misfit.

Let us consider the geometry of the dislocation network displayed in supplementary fig. 1d which is formed by two crossing families of dislocations with axes ξ_1, ξ_2 rotated with respect to the Burgers vectors by the angle α . If α is different from 0 (screw dislocations) and 90° (edge dislocations) both screw and edge components are present. The tensor of plastic deformation for each family reads [1]

$$\beta_k = \begin{pmatrix} 0 & \beta_{\xi_k n} \\ 0 & \beta_{nn} \end{pmatrix}, \quad (\text{S1})$$

where \vec{n} is the vector normal to the dislocation axis, $\beta_{\xi n} = b_\xi / \lambda = b \cos(\alpha) / \lambda$ is the average shear deformation and $\beta_{nn} = b_n / \lambda = b \sin(\alpha) / \lambda$ is the uniaxial expansion/compression. The antisymmetric part of the tensor β determines a rotation of the upper layer with respect to the lower one by a vector $\vec{\omega}$ whereas its symmetric part provides a compensation of the lattice misfit δ

of the layers. Alternative dislocation description was proposed in Ref.[9]; in that model, the conservation of the Burgers vector for each node is provided by involvement of threading (vortex) dislocations resulting in formation of so called “bright stars” and “herringbone” patterns.

To compensate the lattice misfit between graphene and hBN, two families of edge dislocations with the axes perpendicular to the Burgers vectors \vec{b}_1 and \vec{b}_2 are required (Fig. S1c). Reactions between these dislocations also lead to the formation of a hexagonal network (Fig. S1d), which we believe is clearly seen at Fig. 1D of the main text. The complete set of the misfit dislocations can be represented as a superposition of the families of

$$|\vec{\omega}| = \frac{b \cos(\alpha)}{\lambda}, \quad \delta = \frac{b \sin(\alpha)}{\lambda} \quad (\text{S2})$$

At the absence of rotations ($\phi = 0$, $\alpha = 90^\circ$) the inter-dislocation distance is $\lambda = b/\delta$. Oppositely, for a pure rotation of identical layers $2 \sin(\phi/2) = b/d$. At $\delta \neq 0$ additional rotation is required at the angle α determined by the relation

$$\tan(\alpha) = \frac{\delta}{2 \sin(\phi/2)}, \quad (\text{S3})$$

and for the period of the network one has (cf. Ref. [3], Supp Info)

$$\lambda = \frac{b}{\sqrt{\delta(\delta + 2 \sin(\phi/2))}} \quad (\text{S4}).$$

The geometry of the dislocation network is similar the moiré pattern, but the angle α is related with the angle θ of rotation of the moiré pattern used in Ref.[3], Supp Info, Eqs.(3)-(7), by the relation $\theta = 90^\circ - \alpha - \phi$. For graphene-hBN $\delta = (b-a)/a \approx 0.018$ and at $\phi \approx \delta$ the angle θ becomes large. For example, at $\phi = 2.5^\circ$ the angle $\theta = 60.2^\circ$ and $\lambda = 30a$. The essential difference is that in our description all misfit is concentrated in the dislocation cores with a complete lattice conjugation within the hexagonal cells.

To discuss possible reconstructions of the dislocations at the increase of the angle ϕ we need to build an effective one-dimensional potential relief $V(u)$, u is the relative displacement of atomic rows parallel to the dislocation axis. For simplicity, let us consider the case of commensurate periods of superlattice and basic lattice along the dislocation line, with rational $\tan \theta/2$, which leads to rational $\cos \theta$ and $\sin \theta$ and, thus, to commensurability of the dislocation network with crystal lattices. Let integer M be the number of atoms in the dislocation line per elementary cell of the superlattice. The coordinates of these atoms are $\vec{r}_m = m a \vec{e}$ where $m = 0, \dots, M-1$ and $\vec{e} = (\cos \theta, \sin \theta)$ is the unit vector along the dislocation line. For atomic displacement along the line $u \vec{e}$, the potential relief is equal to:

$$V(u) = \frac{1}{M} \sum_{\vec{R}} \sum_{m=0}^{M-1} \varphi(\vec{r}_m - \vec{R} - u \vec{e}) = \frac{1}{M} \sum_{\vec{g}} \varphi_{\vec{g}} \sum_{m=0}^{M-1} e^{i \vec{g} \vec{e} a m} e^{i \vec{g} \vec{e} u} = \frac{1}{M} \sum_{\vec{g}} \varphi_{\vec{g}} \frac{1 - e^{i \vec{g} \vec{e} a M}}{1 - e^{i \vec{g} \vec{e} a}} e^{i \vec{g} \vec{e} u} \quad (\text{S5})$$

where $\varphi(\vec{r} - \vec{R})$ is an interatomic potential between the upper and lower layers, $\varphi_{\vec{g}}$ its Fourier component, $\{\vec{R}\}, \{\vec{g}\}$ are direct and reciprocal crystal lattices for the lower layer. In the two-dimensional Frenkel-Kontorova model [14] we can take into account only minimal \vec{g} -vectors, which are, for triangular Bravais lattice,

$$\vec{g}_1 = \frac{2\pi}{a}(1,0), \quad \vec{g}_2 = \frac{\pi}{a}(-1, \sqrt{3}) \quad (\text{S6})$$

One can see that for small α the potential (S5) is close to a pure cosine whereas for large enough θ it contains several harmonics with comparable coefficients. The shape of oscillations of the potential relief is essentially dependent on θ and M . To illustrate this, we draw just a contribution

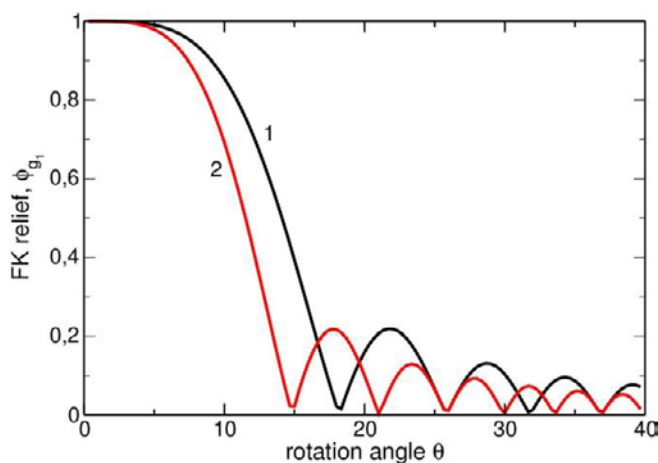


Fig S2 - Dependence of the envelope of potential Frenkel-Kontorova (FK) relief (in the units of ϕ_{g_1}) on the pattern rotation angle θ at $M = 20$ (curve 1) and 30 (curve 2).

proportional to ϕ_{g_1} . Supplementary fig. 2 shows an envelope of oscillations as a function of θ for different M . One can see that the amplitude of the oscillations drops sharply at $\theta \approx 12 - 15^\circ$ decreasing in more than an order of magnitude for $\theta \approx 25^\circ$ and values of M typical for the case of graphene-hBN (see Fig. 1 of the main text).

Within the Frenkel-Kontorova model, the atomic displacements are given by the expression

$$u(x) = 4 \arctan \left[\exp \left(\frac{x - x_0}{\sqrt{K}} \right) \right] \quad (S7)$$

where $K \propto Y / \gamma_{un}$ (Y is the Young modulus, $\gamma_{un} = V_0 / h$ is the unstable stacking fault energy per unit area, V_0 is the amplitude of the potential relief and h is the period in the direction perpendicular to the dislocation axis) [15] which determines the width of the edge dislocation core as

$$\lambda = \frac{a}{2\pi} \sqrt{\frac{Y}{\gamma_{un}}} \quad (S8)$$

(for screw dislocation, Y is replaced by the shear modulus μ). According to the computations, $Y = 22 \text{ eV/\AA}^2$ [16], and, at $\phi = 0$, $\gamma_{un} = 0.004 \text{ eV/\AA}^2$ [13], thus, $\lambda \approx 10a \approx 2.4 \text{ nm}$. After rotation of the graphene layer at $\phi = 2^\circ$ the dislocation network twists at $\theta \approx 25^\circ$ the quantities V_0 and γ_{un} are decreased by an order of magnitude (see Fig. S2) and $\lambda \approx 30a \approx 7.2 \text{ nm}$. Note that in this case $\xi \approx \lambda$ and the whole picture of individual dislocations is no more valid. We believe, however, that this approach is sufficient to predict the breakdown of commensurability and estimate its conditions.

Thus, a smooth increase of misalignment angle $\phi > \delta$, via dramatic increase of the angle θ can result in both decrease of the superlattice period λ and increase of the dislocation-core width, leading to core overlap and commensurate-to-incommensurate transition.

Other examples of samples in commensurate state

Overall we studied over a dozen samples. Below we demonstrate several examples of other device in commensurate state.

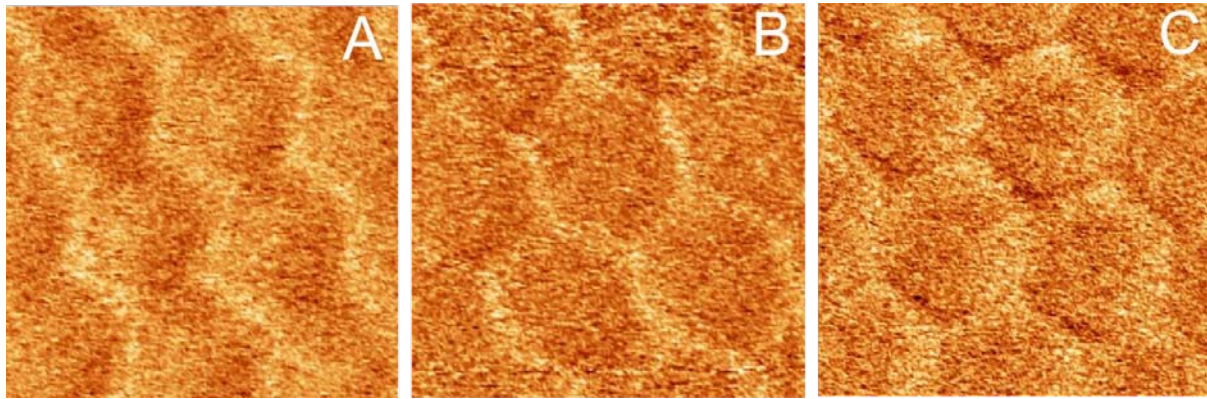


Fig. S3 – (A), (B) and (C) are moiré patterns in Young's modulus for three further fully aligned samples. Each image is 40 x 40 nm.

Details of Scanning tunnelling microscopy (STM) imaging

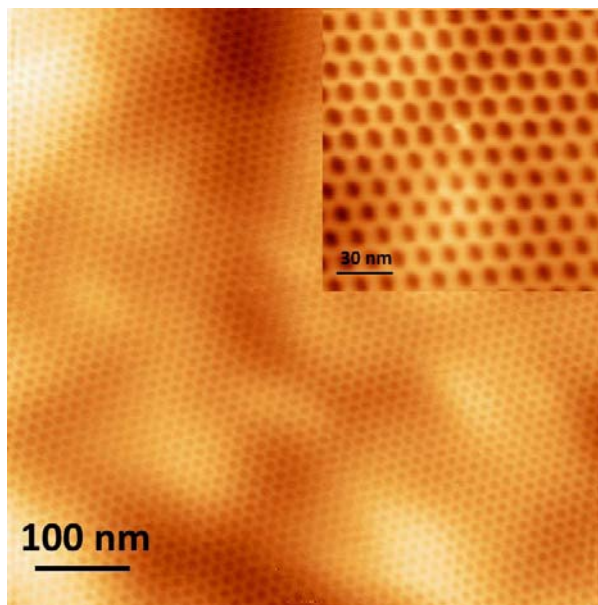


Fig. S4 – moiré superlattice with a 14 nm period.
(Inset) – An enlarged region of the superlattice.

Images were taken of the hBN-graphene superlattice using STM imaging. Fig. S4 shows an image of the moiré superlattice.

Atomic resolution images of the moiré pattern were taken, to establish the variation of graphene's lattice constant across the superlattice period. Fig. S5, demonstrates an atomic resolution image of the pattern.

Fourier transforms of the graphene lattice at various points are taken to compare the graphene lattice constants variation across the superlattice period. Fig. S5 indicates the four regions which are used to extract the Fourier transform. Fig. S6 shows the Fourier transformed images for each of the regions labelled in Fig. S5. Three different directions were used to extract the relative values of

graphene's lattice constant for each region. Only relative values are used because thermal drift distorts the observed graphene lattice. As shown in Fig. S6E,F,G the graphene lattice constant at region A is larger than that of regions B, C, and D.

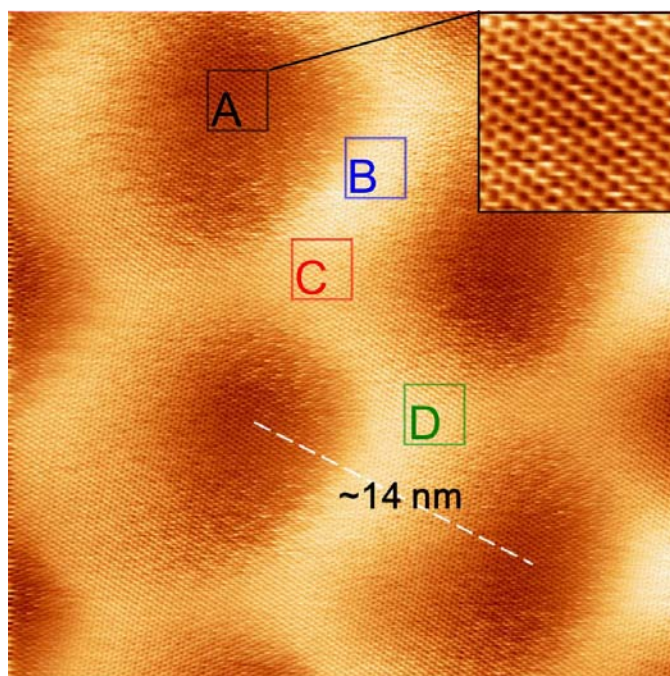


Fig. S5 – A 30x30 nm atomic resolution image of the moiré pattern. **(Inset)** – expanded image of region 1 within the moiré pattern (3x3 nm). Fourier transforms of the regions labelled A, B, C, and D yield the graphene lattice constant at each of these points.

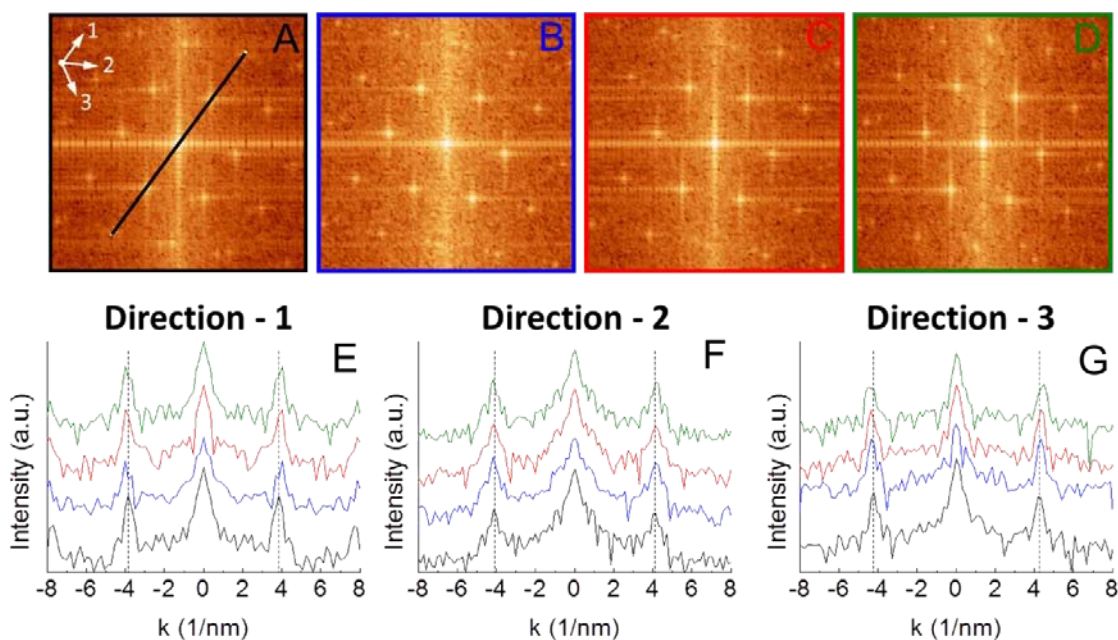


Fig. S6 – **(A-D)** are Fourier transforms of regions A, B, C, and D, (as labelled previously in supplementary figure 5). **(Inset A)** indicates the directions in which the graphene lattice constant is measured in Fourier space. **(E)**, **(F)**, and **(G)** show the signal across the Fourier space in each direction. Dashed lines indicate the peaks corresponding to region A.

- [1] J.P. Hirth and J. Lothe, *Theory of Dislocations* (Krieger Publ., 1982).
- [2] K. Sadananda and M.J. Marcinkowski, J. Appl. Phys. **45**, 1521 (1974).
- [3] M. Yankowitz et al, Nature Phys. **8**, 382 (2012).
- [4] L.A. Ponomarenko et al, Nature **497**, 594 (2013).
- [5] C.R. Dean et al, Nature **497**, 598 (2013).
- [6] B. Hunt et al, Science **340**, 1427 (2013).
- [7] F.C. Frank and J.H. van der Merwe, Proc. R. Soc. A **198**, 205 (1949); *ibid.*, **198**, 216 (1949).
- [8] P. Bak, Rep. Prog. Phys. **45**, 587 (1982).
- [9] C. B. Carter and R. Q. Hwang, Phys. Rev. B **51**, 4730 (1995).
- [10] R. Pushpa and S. Narasimhan, Pure Appl. Chem. **74**, 1663 (2002).
- [11] A. Rockett and C.J. Kiely, Phys. Rev. B **44**, 1154 (1991).
- [12] S.D. Chen, Y.K. Zhou, and A.K. Soh, Comp. Mater. Science **61**, 239 (2012).
- [13] B. Sachs, T. O. Wehling, M. I. Katsnelson, and A. I. Lichtenstein, Phys. Rev. B **84**, 195414 (2011).
- [14] Yu.N. Gornostyrev, M.I. Katsnelson, A.V. Kravtsov, and A.V. Trefilov, Phys. Rev. B **60**, 1013 (1999).
- [15] O.N. Mryasov, Yu.N. Gornostyrev, and A.J. Freeman, Phys. Rev. B **58**, 11927 (1998).
- [16] K.V. Zakharchenko, M.I. Katsnelson, and A. Fasolino, Phys. Rev. Lett. **102**, 046808 (2009).